Supplementary information for: Bidimensional nano-optomechanics and topological backaction in a non-conservative radiation force field

A. Gloppe,[1] P. Verlot,[1] E. Dupont-Ferrier,[1] A. Siria,[2] P. Poncharal,[2] G. Bachelier,[1] P. Vincent,[2] and O. Arcizet[1]

[1]*Institut Néel, Université Grenoble Alpes - CNRS:UPR2940, 38042 Grenoble, France*

[2]*Institut Lumière Matière, UMR5306, CNRS - Université Claude Bernard Lyon 1, 69622 Villeurbanne, France*

Contents

I. EXPANDED EXPERIMENTAL SETUP

Setups shown in Fig. 1 and Fig. 2 of the article are simplified to the minimum information needed to understand the principle of the measurement. In this paragraph, we present a more detailed description of our setup.

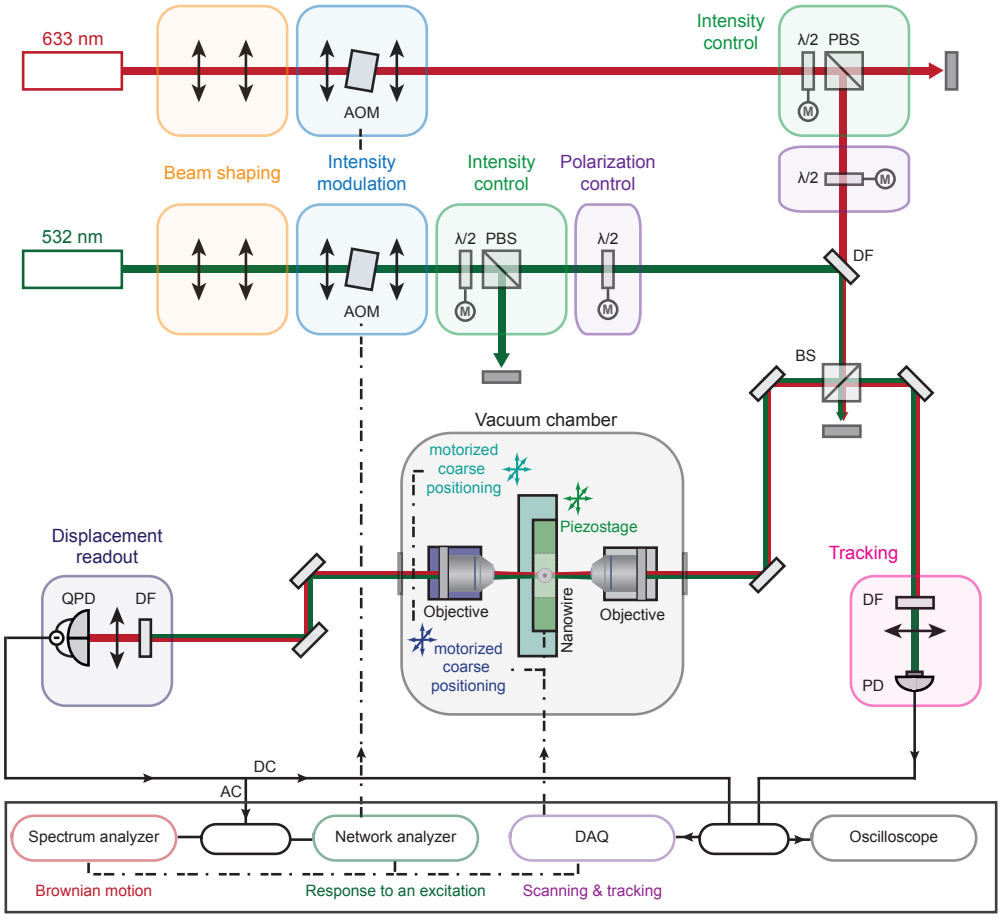

FIG. 1: Scheme of the experiment. *QPD* stands for quadrant photodiode, *PD* for photodiode, *λ/2* for half-wave plate, *PBS* for polarizing beamsplitter, *BS* for beamsplitter, *AOM* for acousto-optic modulator, *DF* for dichroic filter and *DAQ* for the 16-bits data acquisition card which controls the experiment. The configuration shown here is the one used for measuring the green laser force, the red laser being used as a displacement probe, the system spatially tracking the green laser waist ; the roles can be swapped by changing the dichroic filters in front of the *QPD* and the tracking *PD*.

As depicted in Fig. S1, the setup can be divided into principal parts : the laser beams preparation, the vacuum chamber where the light-matter interaction occurs, the tracking module, the displacement readout and the data acquisition system.

The red laser is a low-noise HeNe laser (633 nm). The green laser is a doubled YAG laser (532 nm). We also employed an Oxxius - 405 nm diode laser for further characterization. Each laser is prepared in the same way, first passing through a telescope setup to adapt the beam size and then through an acousto-optic modulator to modulate in intensity the laser beam if necessary. Next, a half-wave plate and a polarizing beamsplitter are used to control the optical power. The half-wave plate can be mounted on a motorized stage to vary the optical power in an automatized way. This is used to perform the optical power ramps in Fig 4. The other port of the beamsplitter is used to monitor the intensity stability of the laser beam as well as its modulation depth. A half-wave plate is employed to control the polarization of each laser beam which are finally combined on a dichroic filter.

The two beams enter the vacuum chamber through an antireflection coated window and are strongly focused by a microscope objective of high numerical aperture (0.75). Symmetrically, the transmitted light is collected through a second similar objective. The second objective is mounted on a translation stage with motorized screws which allows an optimization of the

optical collection when the chamber has been pumped. Note that the microscope objectives are not perfectly corrected for achromatism which leads to a slight shift of 1 μm in the waist position along z between red and green wavelengths. This achromaticity can be advantageously used to spatially discriminate the effects of the pump and probe fields. The nanowire is mounted on a sample holder attached to a piezo-nanopositioning stage mounted on a second motorized translation stage to control the coarse position of the sample with respect to the laser beams. The motorized screws and the piezostage are controlled through a homemade interface program which manages the entire experiment. During measurements, the pump is turned off to avoid unwanted vibrations. A static pressure $< 5 \times 10^{-2}$ mbar can be maintained over one day. The vacuum in the chamber is monitored through a Pirani gauge and can be adjusted with a leak valve (see Sec. III A).

Some measurements require maintaining over long duration (22h for the force map presented in Fig. 2) a spatial consistency which can be limited by the spatial drifts of the system. In order to compensate for these drifts, a routine has been specifically developed using the reflection of the nanowire, propagating through the beamsplitter before the vacuum chamber and imaged on the tracking photodiode. Depending on the laser beam waist on which one wants to spatially lock the experiment, a dichroic filter is placed before the photodiode, to image only the beam of interest. Periodically, approximately every ten minutes the measurement is stopped to compensate for the spatial drifts. Several scans in the XZ and XY planes are performed. The vertical position wanted is retrieved with respect to the end of the nanowire and the position wanted in the optical plane with respect to the optical waist. This allows measurements on very large timescale while keeping the spatial consistency.

A key ingredient of the setup is the quadrant photodiode and its homemade amplifier. The transmistted beam is imaged on the quadrant photodiode after a dichroic filter that selects the probe beam - the one which is not modulated. The balance between the two quadrants is fundamental to cancel potential classical laser noises. During long measurements, the quadrants may get unbalanced. In order to get rid of this issue, the second objective is moved along the transverse direction to balance the quadrants in an automatized way just before the tracking is turned on. The output of the quadrant photodiode is divided into a DC channel and a AC channel. The DC channel (1 kHz cut-off) is used to infer the position of the nanowire with respect to the beam, to balance the quadrants and to determine the measurement vector $\boldsymbol{\beta}$ (see Sec. III C). It is sent on an oscilloscope for live monitoring and on a DAQ card on a computer. The AC channel onto which are imprinted the nanowire vibrations is sent on a power splitter connected to a spectrum analyzer and a network analyzer. The spectrum analyzer is used to measure the Brownian motion of the nanowire. The network analyzer is used to measure the response of the nanowire to the optical excitation both in amplitude - which contains the projected force amplitude, and in phase which contains with the help of the projected measurement vector, the sign of the projected force. All these instruments are controlled through the general data acquisition system.

II. SAMPLES PREPARATION

The silicon carbide nanowires are attached at the extremity of a tungsten wire shaped by electrochemistry into a sharp tip, following the usual procedure used in STM tip fabrication. A carbon glue is employed for adhesion. The mechanical properties of the nanowire are initially measured inside a scanning electron microscope or a transmission electron microscope, by mean of an electrostatic actuation, allowing a measurement of the resonance frequencies and mechanical quality factors. The later can be significantly improved (from approx. 1000 to >10 000) through an in-situ baking procedure between 800°C and 900°C realized by passing a current through the tungsten wire (the temperature is calibrated through the tungsten blackbody emission spectrum). These values persist as long as the vacuum is maintained.

All the experiments reported in this article were done on the same nanowire, presenting a diameter of 150 nm. This work was initially driven by the observation of the topological instability, whose explanation required a precise determination of the optical force field. The nanowire length was initially of $52\,\mu\mathrm{m}$ leading to an oscillation frequency of 113 kHz for the first longitudinal mode family with a 280 Hz splitting. This situation of low frequency and small splitting is indeed favorable for observing the topological instability at low optical powers (approx. $120\,\mu\mathrm{W}$). In order to precisely determine the optical force field topology, it is more convenient to work with large frequency splittings. The nanowire was laser cut down to a length of $25\,\mu\mathrm{m}$, increasing its oscillation frequency up to 264 kHz and the splitting to 900 Hz, a value sufficiently larger than the mechanical linewidth (approx. 100 Hz) to facilitate the force field measurement procedure. When comparing the data before and after the laser cut, the measured changes in effective masses and other geometrical parameters are taken into account. The data presented in Fig. 1bi, Fig. 1c, and Fig. 4 are thus taken with the long nanowire while the shortened nanowire has been employed in Fig. 1bii, Fig. 1d, Fig. 2 and Fig. 3. The laser cut is realized in vacuum by increasing the optical power to several mW and rapidly scanning the nanowire through the focused laser spot at the desired cut height. It permits a sharp cut of the nanowire extremity which does not degrade its mechanical and optical properties and allows to tune with a relatively fine control the nanowire mechanical properties. No degradation of the nanowire mechanical properties were observed after more than one year of operation in vacuum.

III. CHARACTERIZATION OF THE BROWNIAN MOTION

Our setup enables the detection of a single nanowire dynamics. The nanowire is subject to its coupling to the environment and transduces a external applied force into a displacement. In the linear regime, the transduction is linear in the Fourier space such as for one dimension :

$$x[\Omega] = \chi[\Omega](F[\Omega] + F_{\mathrm{T}}[\Omega]) \tag{1}$$

where $x[\Omega]$ is the Fourier component of the nanowire displacement x at a given frequency $\Omega/2\pi$, $\chi[\Omega]$ is the Fourier component of the mechanical susceptibility of the nanowire at this frequency, $F[\Omega]$ is the Fourier component of the external force and F_{T} is the Langevin force resulting from the coupling between the nanowire and a thermal bath. The mechanical susceptibility for a viscously damped harmonic oscillator is written:

$$\chi[\Omega] = \frac{1}{M_{\mathrm{eff}}(\Omega_{\mathrm{m}}^2 - \Omega^2 - i\Omega\Gamma)} \tag{2}$$

with M_{eff} the oscillator effective mass, $\Omega_{\mathrm{m}}/2\pi$ its resonance frequency and Γ its damping rate.

When no external force is applied, one expects to observe only the thermal displacement noise known as Brownian motion induced by the Langevin force which is predicted in terms of spectral density of force by the fluctuation-dissipation theorem :

$$S_{\mathrm{F}}[\Omega] = \frac{2k_{\mathrm{B}}T}{\Omega}\mathrm{Im}\left(-\frac{1}{\chi[\Omega]}\right) = 2M_{\mathrm{eff}}\Gamma k_{\mathrm{B}}T \tag{3}$$

inducing a thermal noise displacement S_{x}:

$$S_{\mathrm{x}}[\Omega] = \mid \chi[\Omega] \mid^2 S_{\mathrm{F}}[\Omega] \tag{4}$$

In this part, we show that the displacement noise observed in our system corresponds to the Brownian motion and that no external noise drives the displacement.

A. Pressure dependence

Increasing the pressure in the vacuum chamber will cause the nanowire damping rate due to the emission of acoustic waves in the surrounding air to increase, and thus the thermal force noise spectral density to be strengthened. We investigate here this mechanism.

The displacement noise spectra of the first mechanical mode for pressures from 5×10^{-3} mbar to 2 mbar are plotted in Fig. S2. The change in pressure is done with the help of a leak valve. The spectra are perfectly fitted with a sum of two uncorrelated lorentzian functions of amplitude at resonance $S_x^i[\Omega_i]$ with i $\in \{1, 2\}$.

These amplitudes and the damping rates Γ_i give access to the displacement variance of each mechanical polarizations. As expected in the case of Brownian motion, the evolution of the displacement variance with the damping rate plotted in Fig. S3 shows no dependence.

Fig. S4 shows the evolution of the damping rate with the pressure. It follows

$$\Gamma_i = \Gamma_i^{\mathrm{int}} + \gamma_i P \tag{5}$$

with Γ_i^{int} the intrinsic damping rate due to clamping and structural losses. The adjustment gives for the first polarization $\Gamma_1^{\mathrm{int}}/2\pi = 61.1$ Hz and $\gamma_1/2\pi = 5.3$ Hz/Pa and for the second polarization $\Gamma_2^{\mathrm{int}}/2\pi = 52.4$ Hz and $\gamma_2/2\pi = 5.6$ Hz/Pa.

B. Brownian motion thermometry

Using a large band gap material such as silicon carbide is a convenient choice for visible light operation. However impurities adsorbed at the surface may be responsible for light absorption. As we use the Brownian motion to calibrate in displacement the response to an applied force, it is crucial to check that there is no heating due to light absorption by the nanowire. A first clue to answer this question is given by the Fig. 1e, where the projected displacement rms amplitude is plotted as a function of the measurement vector angle. As seen in Sec. III E, the variance and thus the mode temperature are constant over the entire measurement area although the intensity seen by the nanowire varies by four orders of magnitude.

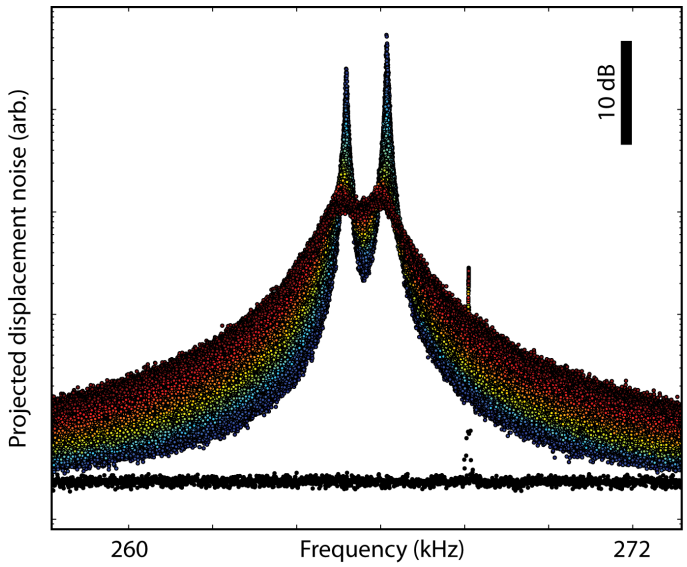

FIG. 2: Displacement noise spectrum before vectorial calibration on the first mechanical mode of the nanowire from 5×10^{-3} mbar (blue) to 2 mbar (red), showing the two mechanical polarizations. The black dots corresponds to the QPD dark noise - RBW = 10 Hz, λ = 633 nm, $P_{opt} = 100\,\mu$W.

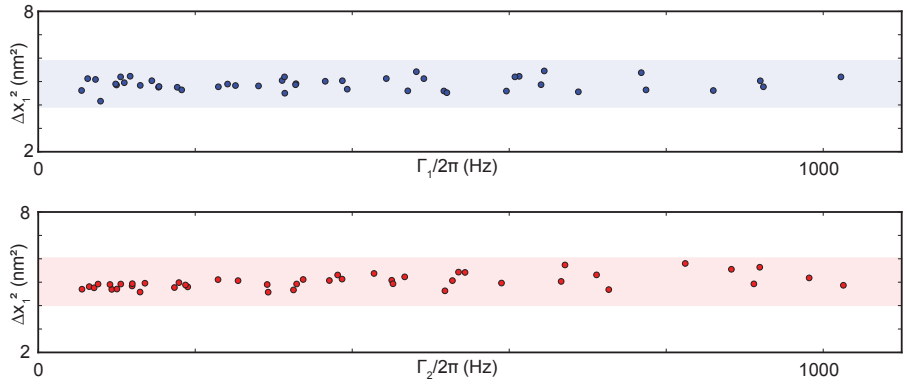

FIG. 3: Evolution of the displacement noise variance with the damping rate for both mechanical polarizations. The bands correspond to $\pm 20\%$ of uncertainty around the mean variance. It shows the independence of the variance with the damping rate as expected by the fluctuation-dissipation theorem.

We consolidate this first clue by perfoming an optical power ramp in the optical waist area with the red laser and check that the variance is optical power independent. The optical polarization is the same as the one used to probe the displacement in the vectorial force map of the Fig. 2 of the article. The green laser is blocked during this experiment. These measurements were performed with the 25 μm long nanowire, presenting increased frequencies and frequencies splitting so that the bifurcation threshold is pushed towards larger optical powers. Furthermore, these measurements are performed on the optical axis, a region of zero vorticity.

The result of this experiment is shown on Fig. S5 where the variance and the damping rate of each mechanical polarizations of the first mechanical mode family are plotted. If there were any absorption, one expect the temperature - or equivalently the noise variance, to increase significantly with the optical power. Here, the optical power, measured before the vacuum chamber, is varied from 20 μW to 200 μW. As a point of reference, the optical power of the red laser used for the force map of Fig. 2 is 86 μW. We show here that there is no increasing trend of the temperature, the variance and the damping rate points being all contained in a ± 10 % band of uncertainty due to a non-perfect determination of the measurement vector. This is a strong evidence of the absence of heating of the nanowire for the optical power employed. Similar measurements conducted in air did not show any detectable temperature increase up to 5 mW.

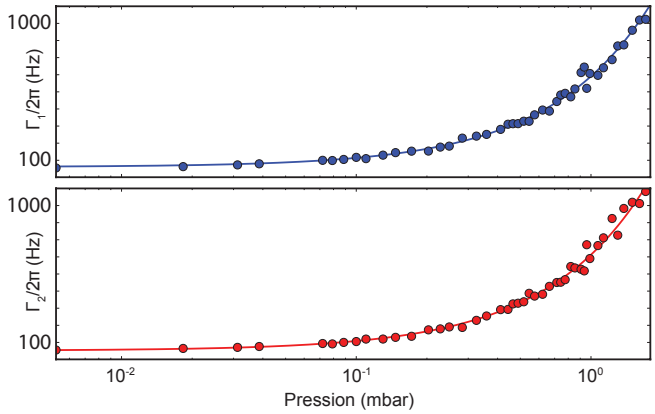

FIG. 4: Evolution of the first mechanical mode damping rate of the nanowire with the pressure for the first mechanical polarization (blue) and for the second mechanical polarization (red) fitted with expression (5).

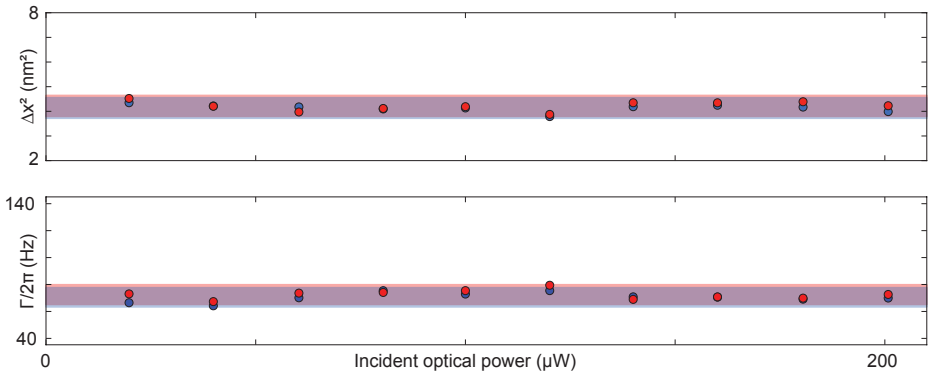

FIG. 5: Displacement variance and damping rate for the two mechanical polarisations (blue and red) on the first mechanical mode as a function of the optical power injected in the vacuum chamber. The bands correspond to $\pm 10\%$ uncertainty (P = 2.1×10^{-2} mbar).

C. Determination of the measurement vector $\boldsymbol{\beta}$

The measurement vector $\boldsymbol{\beta}$ is encapsulating the 2D displacement sensitivity. Its proper characterization is crucial to transduce the output voltage of the photodiode into a displacement. The local tangent plane is measured by moving the piezostage by discrete steps of 25 nm around the working position on a total excursion of 100 nm in $\mathbf{e}_x$ and $\mathbf{e}_z$ directions in nine positions where the static DC voltage of the photodiode is recorded and averaged over 20 ms. A 2D second degree polynomial interpolation is used to determine the measurement vector. This process is averaged over 70 cycles. The same measurement is performed along $\mathbf{e}_x + \mathbf{e}_z$ and $-\mathbf{e}_x + \mathbf{e}_z$ to check the measurement robustness (see Fig. S6).

D. Mechanical profiles

In our system, the optical spot dimensions are always smaller than the typical size over which vary the eigenmode deformation profiles so we can consider conducting out a point-like measurement of the vibration profile [1] as experimentally verified.

For a rectangular beam of length L, the general solution of the dimensionless deformation pattern $u_n(y)$ as a function of the position y along the beam can be written [2] :

$$u_n(y) = A_n \cos(k_n y) + B_n \cosh(k_n y) + C_n \sin(k_n y) + D_n \sinh(k_n y) \tag{6}$$

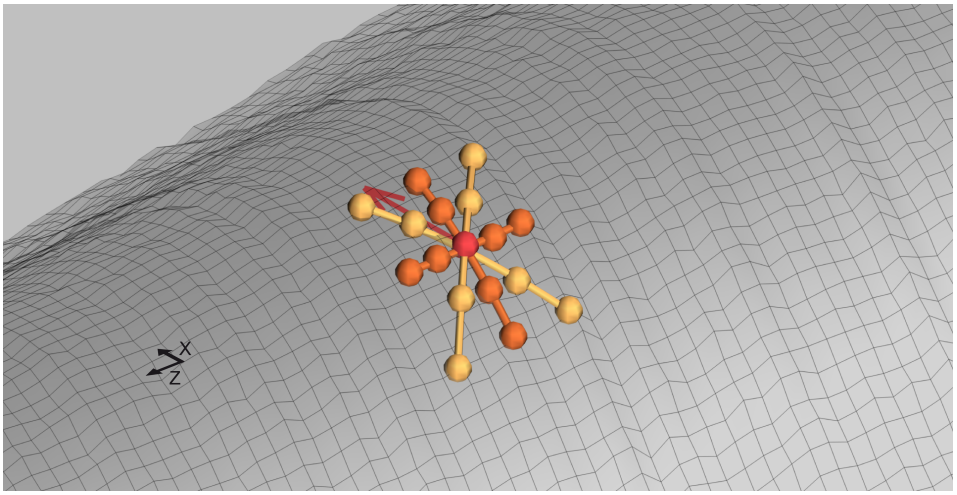

FIG. 6: Principle of the determination of the measurement vector. The DC transmission map of Fig. 1 is zoomed and extruded in wireframe to highlight the 2D transmission variations. For a given working position (red dot), the nanowire is moved along $\mathbf{e}_x$ and $\mathbf{e}_z$ in four different positions (-50 nm, -25 nm, 25 nm, 50 nm) where the static DC voltage of the photodiode is recorded (dark orange dots) - see text for more details. A 2D second degree polynomial interpolation (dark orange lines) is used to determine the measurement vector (red arrow). The same measurement is performed with the basis tilted by 45° to check the measurement robustness (light orange dots and lines).

where n denotes the mechanical mode order, with k_n solution of $\cos(k_n L)\cosh(k_n L) = -1$ and $A_n = -B_n$, $C_n = -D_n$ for a singly clamped beam.

The data presented in the Fig. 1c (iii) inset are measurements of the vibration pattern proportional to $u_n^2(y)$ for the first three mechanical modes obtained by scanning in the XY plane the position of the nanowire and recording the displacement noise power for each mechanical modes. They are fitted using Eq. 6 with a very good agreement with the values expected from the beam theory.

For a given mechanical mode, the kinetic energy is a constant, obtained by integrating the speed of the nanowire along all its length such as

$$E_{\text{cin}} = \frac{1}{2}\rho S \int_0^L \frac{\partial U^2(t,y)}{\partial t} dy$$

where ρ is the nanowire density, S is the nanowire section and $U(t,y) = \delta r(t)\frac{u_n(y)}{u_n(L)}$ with $\delta r(t)$ the temporal evolution of the displacement of the nanowire extremity.

This can be rewritten as a function of $\delta r(t)$ as

$$E_{\text{cin}} = \frac{1}{2}\delta \dot{r}^2(t) M \int_0^L u_n^2(y)/u_n^2(L)\frac{dy}{L}$$

with M being the real mass of the nanowire. We define M_{eff} the effective mass for the given mechanical mode n to plug into the fluctuation-dissipation theorem as

$$M_{\text{eff}} = M \int_0^L u_n^2(y)/u_n^2(L)\frac{dy}{L}$$

The experimental measurement of $u_n^2(y)/u_n^2(L)$ for the first three mechanical modes gives :

$$M_{\text{eff},1} = 0.24M$$
$$M_{\text{eff},2} = 0.26M$$
$$M_{\text{eff},3} = 0.16M$$

E. Effective masses and eigenmodes orientations

Reporting the projected rms amplitude of each mechanical polarizations of the first mechanical mode as a function of the projective measurement angle gives direct access to the eigenmodes orientations. Indeed, for each eigenmode the projected signal displacement will be maximal when the projective measurement angle is aligned with its eigendirection $\mathbf{e}_i$. The rms amplitude data presented in Fig. 1e are adjusted with the angular function $\Delta x_i \mid \mathbf{e}_i \cdot \mathbf{e}_\beta \mid$, leading to

$$\Delta x_1^2 = (1.99\,\mathrm{nm})^2$$
$$\Delta x_2^2 = (1.98\,\mathrm{nm})^2$$

for the noise variances, and

$$\theta_1 = 115.14^\circ$$
$$\theta_2 = 115.98^\circ + 90^\circ$$

We conclude that the two mechanical polarizations are orthogonal, with an angle between $\mathbf{e}_x$ and $\mathbf{e}_1$ $\theta = 115.56^\circ$. The slight deviation from perfect perpendicularity can be explained by the vertical tilt of the nanowire (see section III F). The very good agreement observed over a set of measurement performed over the optical waist area suggests that the nanowire does not experience any measurable heating. The effective masses are the same within the experimental uncertainties for both polarizations. Using T = 300 K, we can deduce the effective mass of the nanowire for the mechanical mode at this particular vertical position through

$$\Delta x^2 = \frac{k_B T}{M_{\mathrm{eff}} \Omega_m^2} \tag{7}$$

and find $M_{\mathrm{eff}} = 376$ fg, 3 μm away from the nanowire extremity. This nanowire has a length of 25 μm and a diameter of 150 nm, modelling it as a perfect cylinder with a density of $\rho = 3210$ kg/m^3 leads to an expected real mass of M = 1418 fg, which means an expected effective mass for the first mode at the extremity of 355 fg. This confirms the quality of the displacement calibration.

F. Role of vertical tilts

The nanowire axis may not be aligned with $\mathbf{e}_y$ but with a tilted vector $\tilde{\mathbf{e}}_y$. The nanowire displacements do not lie in the $(\mathbf{e}_x, \mathbf{e}_z)$ plane but in $(\tilde{\mathbf{e}}_x, \tilde{\mathbf{e}}_z)$ such that $\tilde{B} = (\tilde{\mathbf{e}}_x, \tilde{\mathbf{e}}_y, \tilde{\mathbf{e}}_z)$ is an orthonormal basis. The basis rotation from $B = (\mathbf{e}_x, \mathbf{e}_y, \mathbf{e}_z)$ to $\tilde{B}$ may be written $R = R_\Theta R_\Phi$ with

$$R_\Phi = \begin{pmatrix} \cos\Phi & 0 & \sin\Phi \\ 0 & 1 & 0 \\ -\sin\Phi & 0 & \cos\Phi \end{pmatrix} \quad \text{and} \quad R_\Theta = \begin{pmatrix} \cos\Theta & \sin\Theta & 0 \\ -\sin\Theta & \cos\Theta & 0 \\ 0 & 0 & 1 \end{pmatrix}$$

inducing

$$R = \begin{pmatrix} \cos\Phi\,\cos\Theta & \sin\Theta & \cos\Theta\,\sin\Phi \\ -\cos\Phi\,\sin\Theta & \cos\Theta & -\sin\Phi\,\sin\Theta \\ -\sin\Phi & 0 & \cos\Phi \end{pmatrix}_B$$

The nanowire eigenvectors $\tilde{\mathbf{e}}_i$ lying in the $(\tilde{\mathbf{e}}_x, \tilde{\mathbf{e}}_z)$ plane can be written

$$\tilde{\mathbf{e}}_i = \begin{pmatrix} \cos\tilde{\theta}_i \\ 0 \\ \sin\tilde{\theta}_i \end{pmatrix}_{\tilde{B}}$$

In the base B,

$$\tilde{\mathbf{e}}_i = \begin{pmatrix} \cos\tilde{\theta}_i\,\cos\Phi\,\cos\Theta - \sin\tilde{\theta}_i\,\sin\Phi \\ \cos\tilde{\theta}_i\,\sin\Theta \\ \cos\tilde{\theta}_i\,\sin\Phi\,\cos\Theta + \sin\tilde{\theta}_i\,\cos\Phi \end{pmatrix}_B$$

Measuring the displacement by projecting it in the (e_x, e_z) plane induces an error on the effective masses M_1 and M_2 :

$$\begin{aligned}\frac{\Delta M_i}{M_i} =& 1 - \|\tilde{\mathbf{e}}_i - (\tilde{\mathbf{e}}_i \cdot \mathbf{e}_y)\mathbf{e}_y\|^2 \\ =& \cos^2\tilde{\theta}_i \, \sin^2\Theta\end{aligned}$$

which can only be positive as the displacement can only be underestimated.

The projected and normalized eigenvectors on $(\mathbf{e}_x, \mathbf{e}_z)$ are

$$\mathbf{e_i} = \frac{1}{\sqrt{1-\cos^2\tilde{\theta}_i \, \sin^2\Theta}} \begin{pmatrix} \cos\tilde{\theta}_i \, \cos\Phi \, \cos\Theta - \sin\tilde{\theta}_i \, \sin\Phi \\ 0 \\ \cos\tilde{\theta}_i \, \cos\Theta \, \sin\Phi + \sin\tilde{\theta}_i \, \cos\Phi \end{pmatrix}$$

The apparent tilt θ between $\mathbf{e_1}$ and $\mathbf{e}_x$ is given by

$$\mathbf{e_i} \cdot \mathbf{e}_x = \cos\theta_i = \frac{\cos\tilde{\theta}_i \, \cos\Phi \, \cos\Theta - \sin\tilde{\theta}_i \, \sin\Phi}{\sqrt{1-\cos^2\tilde{\theta}_i \, \sin^2\tilde{\Theta}}}$$

Experimentally, we have access to the angle σ_x between $\tilde{\mathbf{e}}_y$ projected on $(\mathbf{e}_x, \mathbf{e}_y)$ with $\mathbf{e}_y$ and to the angle σ_z between $\tilde{\mathbf{e}}_y$ projected on $(\mathbf{e}_y, \mathbf{e}_z)$ with $\mathbf{e}_y$:

$$\begin{aligned}\cos\sigma_x =& \frac{\cos\Theta}{\sqrt{1-\sin^2\Phi\sin^2\Theta}} \\ \cos\sigma_z =& \frac{\cos\Theta}{\sqrt{1-\cos^2\Phi\sin^2\Theta}}\end{aligned}$$

from which we can deduce experimental values for Θ and Φ :

$$\begin{aligned}\cos^2\Theta =& (\frac{1}{\cos^2\sigma_x} + \frac{1}{\cos^2\sigma_z} - 1)^{-1} \\ \cos^2\Phi =& \frac{\tan^2\sigma_x}{\tan^2\Theta}\end{aligned}$$

Using $\sigma_x = 10.9°$ and $\sigma_z = 2.3°$, it comes $\Phi = 0.3°$ and $\Theta = 10.9°$. The measurement of the apparent angles θ_i (see section III E: $\theta_1 = 115.14°$ and $\theta_2 = 115.98° + 90°$) gives access to the tilt of the eigenvectors in $\bar{B}$ with respect to $\tilde{\mathbf{e}}_x$, confirming the orthogonality of the mechanical polarizations: $\tilde{\theta}_1 = 115.2°$ and $\tilde{\theta}_2 = 115.2° + 90°$. The expected error on the effective masses are 0.6% and 2.9% respectively for the first and the second mechanical polarizations.

IV. LASER INTENSITY NOISE

A. A shot-noise-limited readout

The shot-noise-limited character of the displacement readout can be verified by recording noise spectra at varying optical powers. The measurements were conducted in air, on the first generation of photodiode amplifiers featuring a lower gain suitable for air operation where the absence of topological instability allows to increase significantly the optical power (up to few mW) on the optical axis. The 633 nm laser was employed here.

The signal and measurement background are adjusted with $S_{V_\ominus}[\Omega] = S_V^{\rm bkg} + S_V^{\rm th}\frac{\Omega_{\rm m}^2\Gamma^2}{(\Omega_{\rm m}^2-\Omega^2)^2+\Omega^2\Gamma^2}$ where $S_V^{\rm th}$ and $S_V^{\rm bkg}$ correspond to the peak height of the displacement contribution and to the measurement background. When increasing the injected power P, the transmission gradient also increases. Thus the voltage spectral density corresponding to the Brownian motion scales quadratically with the injected power. This would not be the case if absorption was present in the system, since the temperature of the nanowire would then increase with the optical power. As a consequence a power law larger than P^2 would be expected. When the detection background is shot-noise limited, it is expected to scale linearly with the injected power. These dependencies can be verified in Fig. S7b which shows that no significant heating can be observed in air up to a few mW and that the detection background is quantum limited. Similar measurements were conducted in vacuum (see section III B), where thermalization properties of the nanowire can be expected to be different.

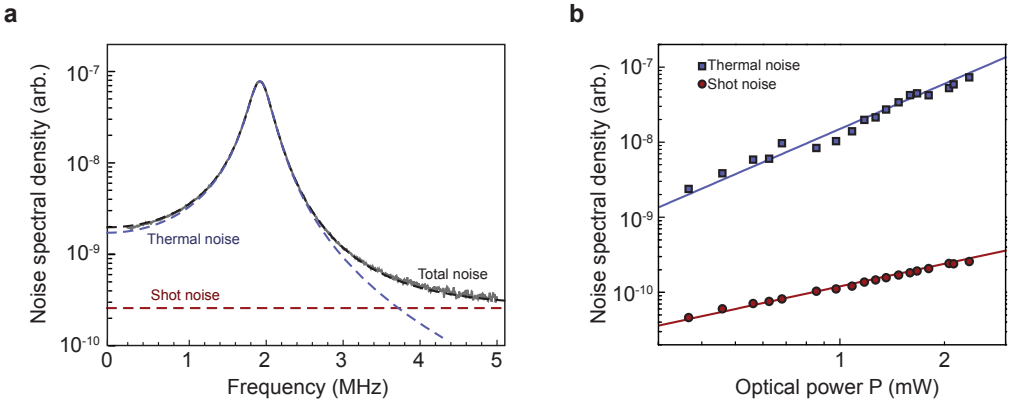

FIG. 7: Power dependence of the displacement noise spectrum and detection background. Measurements were conducted at 633 nm at room pressure on a different nanowire than the one employed in the article, oscillating at 1.96 MHz. For each power P, a spectrum of the QPD differential output is acquired and ajusted with a mechanical Lorentzian added to a flat background (a). The nanowire quality factor is limited to 6.9 in air, so that both polarizations (splitted by 80 kHz) can not be resolved here. The values of the Lorentzian amplitude and of the background after dark noise subtraction are reported as a function of the optical power (b). The detection background presents a linear dependence with P as expected for a shot-noise-limited background. The voltage spectral density corresponding to the thermal noise contribution scales quadratically with P, underlying the absence of detectable heating, up to a few mW.

B. Force noise induced by the green laser intensity noise

The red probe laser is shot-noise-limited at the frequency studied for the detection optical power. The green laser presents a larger classical intensity noise which we quantify here. The spectral density of the Langevin force for a typical nanowire is compared to the spectral density of the optical force noise generated by the green laser intensity noise to check that this optical force noise is negligible in our problem.

The intensity of the laser is varied from 30 μW to 100 μW using a motorized half-wave plate and a polarizing beam splitter. The calibration of the wave-plate angle with the optical power incoming on the photodetector is done prior to the measurement set. The laser intensity noise S_P is then recorded for different optical powers on the spectrum analyzer (RBW = 51 Hz), the photodetector gain and transfer function being known. The intensity noise on 50 kHz around 265 kHz reachs a maximal value of 7 nW^2/Hz for 100 μW incoming on the detector.

The order of magnitude for optical forces induced by a 1 mW laser beam is 1 pN. This figure of merit is used to transduce the laser intensity noise on this frequency range into a force spectral density of $(2.7\ \mathrm{aN})^2/\mathrm{Hz}$ which has to be compared with a typical spectral density of the Langevin force of $(30\ \mathrm{aN})^2/\mathrm{Hz}$ for the studied nanowires. This shows that the laser intensity noise is responsible for an effective equivalent bath temperature representing less than 1% of the Langevin temperature on this frequency range.

V. TOPOLOGICAL BIFURCATION WITH THE GREEN LASER

The data presented in Fig. 4 are obtained with the optical force field apply by the red laser - the green laser being switched off. As the force fields generated by both colors have similar topology, we could observe the same kind of topological bifurcation with the green laser, the red laser being switched off. Fig. S8 shows a typical evolution of the displacement spectrum while the green optical power is ramped up, the nanowire being in a topologically unstable region.

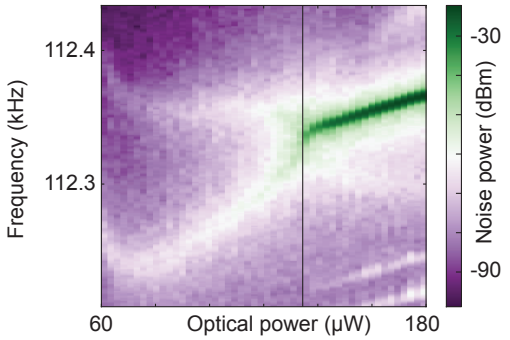

FIG. 8: Typical evolution of the displacement noise spectrum as a function of the incident optical power in the topologically unstable region for the green laser (RBW = 4.3 Hz).

VI. FORCE INDUCED BY THE RED LASER

The vectorial force map presented in Fig. 2 and exploited in Fig. 3 represents the optical force field applied by a green laser (532 nm) on the nanowire. The experiment is conducted by modulating the intensity of the green laser through an acousto-optic modulator while probing the displacement of the nanowire with the red laser (633 nm). The role of each beam can be inverted in order to quantify the dynamical backaction due to the red laser in Fig. 3 and to investigate the wavelength dependence of the light-matter interaction at the nanoscale.

We measured the vectorial force map (Fig. S9b) induced by the red laser by modulating its intensity with another acousto-optic modulator, while the green laser is used as the displacement probe. The optical polarizations used are the same as the force map of Fig. 2. The tracking system is now centered on the red laser waist. We scan a region of 2.5 x 3 μm^2 over 36 hours (30x29 points with a 24s averaging time on the VNA and a 15s averaging time on the SA).

The force map shows a maximum value of 3.26 fN for a intensity modulation depth of 44 % with a mean optical power of 50 μW, corresponding to 14.2 fN for a full-depth modulation of 96 μW injected in the vacuum chamber. The frequency splitting between the two mechanical polarizations is plotted in Fig. S9b. It highlights that the optical force field induced by the red laser for this optical polarization generates a negligible dynamical backaction compared to the optical force field induced by the green laser which has its waist at the bottom of the scan area. The red laser can be considered a non-perturbing displacement probe.

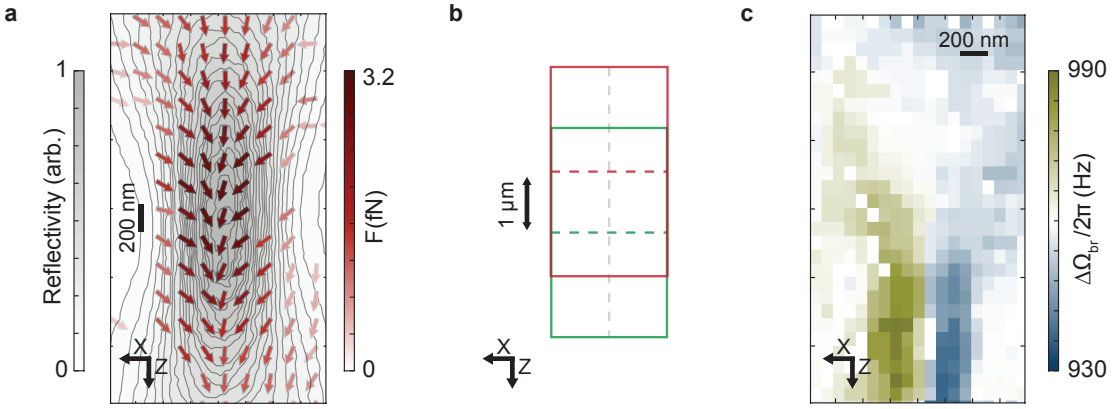

FIG. 9: (a) Vectorial map of the optical force field induced by the red laser with the same optical polarization as in the measurement leading to Fig. 2, with the green laser being used as the displacement probe. (b) Schematic showing the displayed scan area for this measurement locked on the red laser waist with respect to the measurement shown in Fig. 2 locked on the green laser waist. (c) Frequency splitting between the two mechanical polarizations of the first mode family Brownian motion spectra. The measurement is centered on the red laser waist and shows that the dynamical backaction on the nanowire is dominated by the optical force field applied by the green laser.

VII. EVOLUTION OF THE FREQUENCY SPLITTING WITH THE OPTICAL POLARIZATION

Fig. 4g shows the evolution of the frequency splitting between both mechanical polarizations of the first mechanical mode as a function of the optical polarization, for three different positions in the optical waist. It illustrates the strong dependence of the optomechanical interaction on the optical polarization.

For a given optical polarization of the red laser - the green one being switched off, the nanowire is moved over 2 μm across the optical axis in 500 different positions. A spectrum centered on the first mechanical modes is recorded in each position, for a total acquisition time of roughly 10 minutes for each optical polarization. The optical polarization is adjusted by mean of a half-wave plate, without modifying the incoming optical power in the vacuum chamber fixed at 350 μW.

The spatial drifts occuring between each measurement are readjusted with the help of the minimum of sensitivity. Fig. S10 shows the resulting density plots zoomed on the zone of interest between 111.77 kHz and 113.77 kHz. The signal-to-noise is enhanced - at constant optical power - when the electric field is aligned with the nanowire axis.

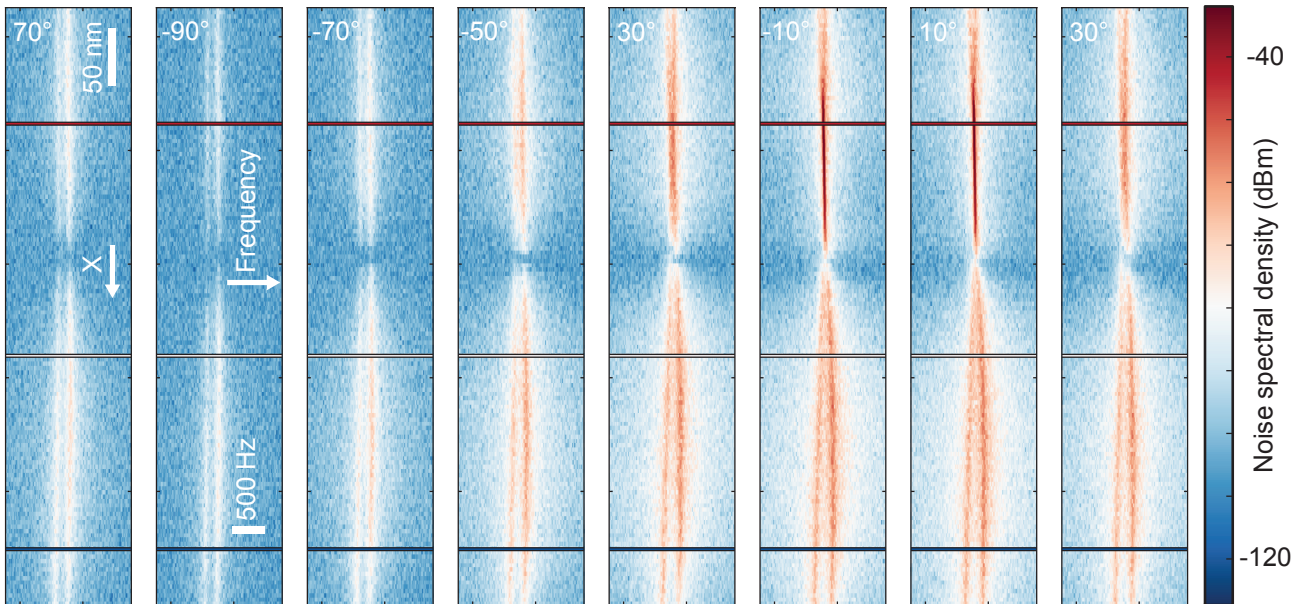

FIG. 10: Spatial maps of the displacement spectra acquired while scanning the nanowire across the optical axis close to the optical waist for different optical polarizations of the red probe laser, showing the polarization dependence of the optomechanical interaction at the nanoscale and thus of the topological backaction. The three different positions used in Fig. 4g are reported in red, white and dark blue respectively.

In the Fig. 4g of the main text, the frequency splitting between both mechanical polarizations are reported as a function of the light polarization angle in three differents transverse positions. These positions are marked on Fig. S10 with the same colors as they appeared in the original figure. The frequency splitting is adjusted for each spectrum. The polarization presenting a large signal-to-noise ratio is also the one for which the topological instability is maximum.

We take advantage of this easily-accessible degree of freedom to minimize the topological backaction due to the red laser when using it as displacement probe, in particular for measuring the vectorial force map of Fig. 2.

VIII. FORMALIZATION

A. Nanowire dynamics in the optical force field

Linearizing the equations of motion around the oscillator rest position $\mathbf{r_0}$ and going to the Fourier domain allows to compute the position fluctuations $\delta\mathbf{r}[\Omega]$ in presence of optical gradient forces, expressed in the ($\mathbf{e}_1$,$\mathbf{e}_2$) basis:

$$\bar{\chi}[\Omega]^{-1} \cdot \begin{pmatrix} \delta r_1[\Omega] \\ \delta r_2[\Omega] \end{pmatrix} = \begin{pmatrix} \delta F^1_{\rm th}[\Omega] \\ \delta F^2_{\rm th}[\Omega] \end{pmatrix}$$

with

$$\bar{\chi}[\Omega]^{-1} = M \begin{pmatrix} \Omega_1^2 - \Omega^2 - i\Gamma_1\Omega - g_{11} & -g_{21} \\ -g_{12} & \Omega_2^2 - \Omega^2 - i\Gamma_2\Omega - g_{22} \end{pmatrix}$$

so that the modified mechanical susceptibility in 2D, $\bar{\chi}[\Omega]$ follows

$$\begin{pmatrix} \delta r_1[\Omega] \\ \delta r_2[\Omega] \end{pmatrix} = \bar{\chi}[\Omega] \cdot \begin{pmatrix} \delta F^1_{\rm th}[\Omega] \\ \delta F^2_{\rm th}[\Omega] \end{pmatrix}$$

with

$$\bar{\chi}[\Omega] = \frac{1}{\Xi[\Omega]} \begin{pmatrix} \Omega_2^2 - \Omega^2 - i\Gamma_2\Omega - g_{22} & g_{21} \\ g_{12} & \Omega_1^2 - \Omega^2 - i\Gamma_1\Omega - g_{11} \end{pmatrix}$$

and

$$\Xi[\Omega]/M = (\Omega_1^2 - \Omega^2 - i\Gamma_1\Omega - g_{11})(\Omega_2^2 - \Omega^2 - i\Gamma_2\Omega - g_{22}) - g_{12}g_{21}$$

As a consequence, at large optical power the intial Langevin forces are driving both vibration axis and the vibrations along the initial eigendirections $\mathbf{e_{1,2}}$ are correlated.

B. Eigenmodes

The restoring force matrix $\mathbf{\Omega^2} = \bar{\chi}[0]^{-1}/M$ can be diagonalized to compute the eigenfrequencies $\Omega_\pm$ and eigenvectors $\mathbf{e}_\pm$:

$$\Omega_\pm^2 \equiv \frac{\Omega_1^2 + \Omega_2^2 - g_{11} - g_{22}}{2} \pm \frac{1}{2}\sqrt{(\Omega_1^2 - \Omega_2^2 + g_{22} - g_{11})^2 + 4g_{21}g_{12}}$$

Note that the gradients terms ($g_{ij} \equiv P\gamma_{ij}$) are taken along the eigenmodes axes in absence of light. When the optical forces vanish ($g_{ij} \to 0$), which is the case at low light power but also far away from the waist region, if $\Omega_1 < \Omega_2$ then $\Omega_- \to \Omega_1$ and $\Omega_+ \to \Omega_2$. Their expansion up to the second order in P:

$$\begin{aligned} \Omega_+^2 &\approx \Omega_2^2 - \gamma_{22}P + \tfrac{\gamma_{12}\gamma_{21}}{\Omega_2^2 - \Omega_1^2}P^2 \\ \Omega_-^2 &\approx \Omega_1^2 - \gamma_{11}P - \tfrac{\gamma_{12}\gamma_{21}}{\Omega_2^2 - \Omega_1^2}P^2 \end{aligned}$$

The unitary eigenvectors $\mathbf{e}_\pm$ are

$$\mathbf{e}_- = \frac{1}{\sqrt{g_{12}^2 + (\Omega_{2\|}^2 - \Omega_-^2)^2}} \begin{pmatrix} \Omega_{2\|}^2 - \Omega_-^2 \\ g_{12} \end{pmatrix}$$

$$\mathbf{e}_+ = \frac{1}{\sqrt{g_{21}^2 + (\Omega_+^2 - \Omega_{1\|}^2)^2}} \begin{pmatrix} -g_{21} \\ \Omega_+^2 - \Omega_{1\|}^2 \end{pmatrix}$$

where we have introduced $\Omega_{i\|}^2 = \Omega_i^2 - g_{ii}$. One can notice that $\Omega_{2\|}^2 - \Omega_-^2 = \Omega_+^2 - \Omega_{1\|}^2 = \Delta\Omega_\|^2/2 + \frac{1}{2}\sqrt{\Delta\Omega_\|^4 + 4g_{12}g_{21}}$ with $\Delta\Omega_\|^2 = \Omega_{2\|}^2 - \Omega_{1\|}^2$.

Their scalar product is:

$$\mathbf{e}_+ \cdot \mathbf{e}_- = \frac{g_{12} - g_{21}}{2} \frac{\Delta\Omega_\parallel^2 + \sqrt{\Delta\Omega_\parallel^4 + 4g_{12}g_{21}}}{\sqrt{(g_{21}^2 + (\Omega_{1\parallel}^2 - \Omega_+^2)^2)(g_{12}^2 + (\Omega_{2\parallel}^2 - \Omega_-^2)^2)}}$$

In the case of a conservative force field, the restoring force matrix is symmetric and the eigenvectors are perpendicular to each others. On the contrary, when the force field has a non-conservative character, the eigenvectors are not perpendicular anymore. Beyond the bifurcation, the eigenvectors acquire an imaginary part, so that the eigen trajectories become elliptical.

C. Projected displacement noise

The projective readout works as $\delta r_\beta[\Omega] = \mathbf{e}_\beta \cdot \delta\mathbf{r}[\Omega] \equiv \delta_1[\Omega]\cos\theta_\beta + \delta_2[\Omega]\sin\theta_\beta$, with $\cos\theta_\beta = \mathbf{e_1} \cdot \mathbf{e}_\beta$, so that:

$$\delta r_\beta[\Omega] = \cos\theta_\beta(\bar{\chi}_{11}[\Omega]\delta F_1[\Omega] + \bar{\chi}_{12}[\Omega]\delta F_2[\Omega]) + \sin\theta_\beta(\bar{\chi}_{21}[\Omega]\delta F_1[\Omega] + \bar{\chi}_{22}[\Omega]\delta F_2[\Omega])$$

The corresponding spectral noise density is:

$$\begin{aligned} S_{\delta r_\beta}[\Omega] = \frac{1}{|\Xi[\Omega]|^2}\Big[& \cos^2\theta_\beta \left(((\Omega_{2\parallel}^2 - \Omega^2)^2 + \Omega^2\Gamma_2^2)S_{\mathrm{F}_1} + g_{21}^2 S_{\mathrm{F}_2}\right) \\ & + \sin^2\theta_\beta \left(g_{12}^2 S_{\mathrm{F}_1} + ((\Omega_{1\parallel}^2 - \Omega^2)^2 + \Omega^2\Gamma_1^2)S_{\mathrm{F}_2}\right) \\ & + \sin 2\theta_\beta \left(g_{12}(\Omega_{2\parallel}^2 - \Omega^2)S_{\mathrm{F}_1} + g_{21}(\Omega_{1\parallel}^2 - \Omega^2)S_{\mathrm{F}_2}\right)\Big] \end{aligned}$$

IX. ANALYSIS OF THE TOPOLOGICALLY UNSTABLE AREA

Here we analyze the spatial shape of the area where the bifurcation and the topological instability occur.
We introduce the discriminant of the restoring force matrix as

$$D(\mathbf{r}, P) \equiv \Delta^2 - 2\Delta P f(\mathbf{r}) + P^2 h(\mathbf{r})$$

with $\Delta \equiv \Omega_1^2 - \Omega_2^2$, $f(\mathbf{r}) = \gamma_{11} - \gamma_{22}$ and $h(\mathbf{r}) = (\gamma_{11} - \gamma_{22})^2 + 4\gamma_{12}\gamma_{21}$. At low power, the discriminant is positive in any point in space. There exists a position $\mathbf{r_0} = (x_0, z_0)$ where the bifurcation first appears, corresponding to $\Delta\Omega = 0$ at a power P_0 which fulfills:

$$D(\mathbf{r_0}, P_0) = 0 \,\text{and}\, \nabla D(\mathbf{r}, P_0)|_{\mathbf{r_0}} = \mathbf{0}.$$

Here we assume that the instability appears in one single point. The expression for the bifurcation threshold is

$$P_0 = (\Omega_2^2 - \Omega_1^2)\frac{\gamma_{11} - \gamma_{22} + 2\sqrt{-\gamma_{21}\gamma_{12}}}{-(\gamma_{22} - \gamma_{11})^2 - 4\gamma_{21}\gamma_{12}}$$

which increases with the cold frequency splitting $\Delta\Omega_0$. Note that this expression holds in regions of permanent instability above threshold, where $-(\gamma_{22} - \gamma_{11})^2 - 4\gamma_{21}\gamma_{12} > 0$.

There also exists a point $\mathbf{r_1}$ where the topological instability first appears at a power P_1, corresponding to $\mathrm{Im}(\Delta\Omega) = 1/2\bar{\Omega}\sqrt{|\mathrm{D}(\mathbf{r_1}, \mathrm{P_1})|} = -\Gamma$ which corresponds to:

$$D(\mathbf{r_1}, P_1) = -4\Gamma^2\bar{\Omega}^2 \,\text{and}\, \nabla D(\mathbf{r}, P_1)|_{\mathbf{r_1}} = \mathbf{0}. \tag{8}$$

In general the points $\mathbf{r_0}$ and $\mathbf{r_1}$ can be spatially separated. However, in the limit of large quality factors ($\Gamma \to 0$), one expects $P_1 \to P_0$ and $\mathbf{r_1} \to \mathbf{r_0}$.

For the bifurcation criteria, these conditions give

$$\Delta^2 - 2\Delta P_0 f_0 + P_0^2 h_0 = 0 \,\text{and}\, 2\Delta\ \nabla f|_{\mathbf{r_0}} = P_0\ \nabla h|_{\mathbf{r_0}}$$

Then, the boundary of the bifurcated region can be computed by exploring the locations $\mathbf{r_0} + \boldsymbol{\delta}\mathbf{r}$ where the discriminant is zero for a slightly larger optical power $P_o + \delta P$:

$$D(\mathbf{r_0} + \boldsymbol{\delta}\mathbf{r}, P_o + \delta P) = 0 \tag{9}$$

In order to calculate the shape and the area of the bifurcated region, we will expand the position at second order in $\boldsymbol{\delta}\mathbf{r}$ and the optical power at first order in δP. The second order spatial expansion of the functions f and h is written:

$$g(\mathbf{r_0} + \boldsymbol{\delta}\mathbf{r}) \approx g_0 + (\boldsymbol{\delta}\mathbf{r} \cdot \nabla)g + \frac{\delta_x^2}{2}\,\partial_{xx}g + \delta_x\delta_z\,\partial_{xz}g + \frac{\delta_z^2}{2}\,\partial_{zz}g$$

Then after simplification, Eq. 9 becomes:

$$\left\{\frac{\delta_x^2}{2}\partial_{xx} + \frac{\delta_z^2}{2}\partial_{zz} + \delta_x\delta_z\partial_{xz}\right\}\left(-2\Delta P_0 f + P_0^2 h\right) + \left\{\delta_x\partial_x + \delta_z\partial_z + 1\right\}\left(P_0 h - \Delta f\right)2\delta P = 0$$

This is the equation of an ellipse, in a referential (x, z) which is not aligned with its eigen axis:

$$\alpha_{xx}\delta_x^2 + \alpha_{zz}\delta_z^2 + \alpha_{xz}\delta_x\delta_z + \beta_x\delta_x + \beta_z\delta_z + \gamma = 0$$

It can be expressed in the base (u, v) obtained by rotating the (x, z) basis by an angle Θ in order to cancel the cross-term uv, such that:

$$\tan 2\Theta = \frac{\alpha_{xz}}{\alpha_{xx} - \alpha_{zz}}$$

This basis is aligned with the eigen directions of the ellipse. In this new basis, the equation of the ellipse becomes:

$$\alpha_{uu}\delta_u^2 + \alpha_{vv}\delta_v^2 + \beta_u\delta_u + \beta_v\delta_v + \gamma = 0$$

with:

$$\begin{aligned}
\alpha_{uu} &= \alpha_{xx}\cos^2\Theta + \alpha_{xz}\cos\Theta\sin\Theta + \alpha_{zz}\sin^2\Theta \\
\alpha_{vv} &= \alpha_{xx}\sin^2\Theta - \alpha_{xz}\cos\Theta\sin\Theta + \alpha_{zz}\cos^2\Theta \\
\beta_u &= \beta_x\cos\Theta + \beta_z\sin\Theta \\
\beta_v &= -\beta_x\sin\Theta + \beta_z\cos\Theta \\
\gamma &= 2\delta P(P_0h_0 - \Delta f_0)
\end{aligned}$$

and

$$\begin{aligned}
\alpha_{xx} &= \partial_{xx}\left(-2\Delta P_0 f + P_0^2 h\right)/2 \\
\alpha_{zz} &= \partial_{zz}\left(-2\Delta P_0 f + P_0^2 h\right)/2 \\
\alpha_{xz} &= \partial_{xz}\left(-2\Delta P_0 f + P_0^2 h\right) \\
\beta_x &= 2\delta P\,\partial_x(P_0h - \Delta f) \\
\beta_z &= 2\delta P\,\partial_z(P_0h - \Delta f)
\end{aligned}$$

Then the equation of the ellipse can be written:

$$\frac{(\delta_u - u_0)^2}{a^2} + \frac{(\delta_v - v_0)^2}{b^2} = 1$$

where a and b are the radii of the ellipse of area πab and center (u_0, v_0) in the (u,v) basis. We define

$$K \equiv \beta_u^2/4\alpha_{uu} + \beta_v^2/4\alpha_{vv} - \gamma$$

such that $a = \sqrt{K/\alpha_{uu}}$, $b = \sqrt{K/\alpha_{vv}}$ and $(u_0, v_0) = (-\beta_u/2\alpha_{uu}, -\beta_v/2\alpha_{vv})$.

Thus, the area of the ellipse $S = \pi ab$ can be written:

$$S_0 = \pi\sqrt{\frac{K^2}{\alpha_{uu}\alpha_{vv}}}$$

The ellipse discriminant is invariant by basis rotation : $\alpha_{uu}\alpha_{vv} = \alpha_{xx}\alpha_{zz} - \alpha_{xz}^2/4 > 0$. At first order in $\delta P(>0)$, $K^2 \approx \gamma^2$ and one obtains:

$$S_0(\delta P) = \pi\frac{2|P_0h_0 - \Delta f_0|}{\sqrt{\alpha_{xx}\alpha_{zz} - \alpha_{xz}^2/4}}\delta P$$

which presents a linear dependence in $\delta P = P - P_0$. It can also be written,

$$S_0(P) = 2\pi(P - P_0)\left.\frac{|\,\partial_P D\,|}{\sqrt{\partial_{xx}D.\partial_{zz}D - \partial_{xz}D.\partial_{xz}D}}\right|_{\mathbf{r_0},P_0}$$

The same reasoning can be developed to calculate the evolution of the instability area $S_1(P)$ for optical powers beyond P_1:

$$S_1(P) = 2\pi(P - P_1)\left.\frac{|\,\partial_P D\,|}{\sqrt{\partial_{xx}D.\partial_{zz}D - \partial_{xz}D.\partial_{xz}D}}\right|_{\mathbf{r_1},P_1}$$

Assuming that the position at which the bifurcation and the instability first occur are identical ($\mathbf{r_0} = \mathbf{r_1}$), one has:

$$P_1 \approx P_0 + \frac{4\bar{\Omega}^2\Gamma^2}{-\,\partial_P D|_{\mathbf{r_0},P_0}}$$

($\partial_P D|_{\mathbf{r_0},P_0} < 0$) so that at first order in $\Gamma^2 = \bar{\Omega}^2/Q^2$, one has:

$$S_1(P) = 2\pi\left(P - P_0 - \frac{4\bar{\Omega}^4/Q^2}{-\,\partial_P D|_{\mathbf{r_0},P_0}}\right)\left.\frac{|\,\partial_P D\,|}{\sqrt{\partial_{xx}D.\partial_{zz}D - \partial_{xz}D.\partial_{xz}D}}\right|_{\mathbf{r_0},P_0} \tag{10}$$

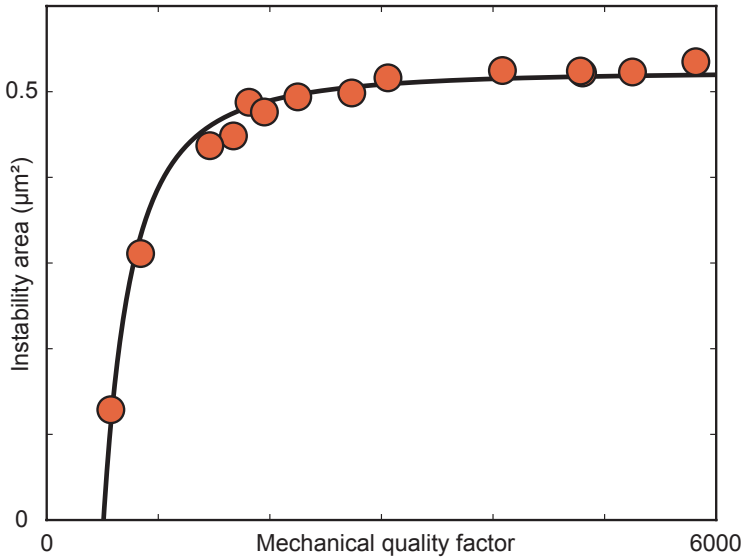

FIG. 11: Evolution of the instability area at a given optical power ($P_{\rm opt} = 301\ \mu$W) as a function of the intrinsic quality factor. This shows indirectly the dependence of the optical threshold with the nanowire intrinsic damping rate. The experimental data are fitted with expression (10).

The quality factor can be varied by changing the pressure in the vacuum chamber. Fig S11 shows the dependence of the unstable area on the intrinsic quality factors for a constant optical power $P = 301\ \mu$W beyond the threshold. The intrinsic quality factor is measured outside the topological instability area. The data are fitted with expression (10).

[1] M. Pinard, Y. Hadjar, and A. Heidmann, The European Physical Journal D - Atomic, Molecular, Optical and Plasma Physics **7**, 107 (1999), ISSN 1434-6060, URL http://dx.doi.org/10.1007/s100530050354.

[2] A. Cleland, *Foundations of Nanomechanics: From Solid-State Theory to Device Applications*, Advanced Texts in Physics (Springer, 2003), ISBN 9783540436614.